Acta Materialia 298 (2025) 121393

Contents lists available at ScienceDirect

Acta Materialia

journal homepage: www.elsevier.com/locate/actamat

Full length article

Scaling behavior of Poisson's ratio in hierarchical nanoscale network materials

Haonan Sun [a], Lukas Lührs [b], Wei-Che Chang [c], Shan Shi [a,c,*]

[a] Research Group of Integrated Metallic Nanomaterials Systems, Hamburg University of Technology, Hamburg, Germany
[b] Institute of Materials Physics and Technology, Hamburg University of Technology, Hamburg, Germany
[c] Institute of Hydrogen Technology, Helmholtz-Zentrum Hereon, Geesthacht, Germany

ARTICLE INFO

Keywords:
Nanoporous metals
Poisson's ratio
Hierarchical structure
Scaling law
Mechanical properties

ABSTRACT

Hierarchical nanoscale network materials have gained increasing interest over the last decade attributing to their enhanced functional and mechanical performance, combined with reduced density. However, investigations into their Poisson's ratio, a key fundamental mechanical property, remain lacking. In this work, monolithic hierarchical nanoporous gold with tunable structure size and solid volume fraction were prepared via a two-step electrochemical dealloying method. By using in-situ digital image correlation technique, we measured their elastic and plastic Poisson's ratios during macroscopic compression. The effects of solid fraction, upper level ligament size and strain were explored systematically. We found that both the elastic and plastic Poisson's ratios are independent of the upper level ligament size and compressive strain. Notably, we introduced a novel scaling law of elastic Poisson's ratio with solid fraction in hierarchical nanoscale network materials and verified it experimentally. This study addresses a knowledge gap in the mechanics of hierarchical nanoscale network materials, offering a comprehensive understanding of their structure–mechanical property relationships. This insight provides a foundation for the design of novel materials and the optimization of their functional and mechanical properties.

1. Introduction

Nanoporous gold (NPG) with bicontinuous network structure made by electrochemical or chemical dealloying has served as a model material system to study the relationships between microstructure and mechanical properties (such as stiffness, strength and Poisson's ratio) in nanoscale network materials. This is attributed to its facile fabrication, high chemical resistance and tunable structure parameters such as ligament size and solid fraction [1–9]. Moreover, understanding the mechanical properties of nanoporous metals is essential to optimize their performances in various applications such as lightweight structural materials, actuators, strain sensors and catalysts [10,11].

Beyond unimodal nanoporous metals, nanoporous metals with hierarchical structure (e.g., two or three well-defined ligament/pore sizes) have attracted increasing attentions in the last two decades [12–21]. This is because the large pores at upper hierarchical levels are beneficial for fast mass transport and small pores at lower hierarchical levels for a large surface-to-volume ratio, thus providing an efficient approach for optimizing functional performances in various applications such as batteries, supercapacitors and fuel cells. Recently, the successful fabrication of crack-free macroscopic hierarchical nanoporous gold (HNPG) with independently tunable structure size and solid fraction at two hierarchical levels [19,20] has opened the door to study the mechanics of such a class of materials via conventional mechanical testing methods. This allows HNPG to serve as a model material system to understand the fundamental structure–mechanical properties in hierarchical nanoscale network materials in general. For instance, mechanical studies on HNPG demonstrated that structural hierarchy can lead to enhanced specific stiffness and strength of network materials at the nanoscale and simultaneously reduced densities. Moreover, ligament size effect at each hierarchical level and quantitative scaling equations between stiffness/strength and solid fraction have already been explored [19,21]. However, studies on Poisson's ratio ν, a material property that complements Young's modulus in describing the elastic behavior of materials under stress, remain absent. ν quantifies the deformation of a material in directions perpendicular to the applied force and can be expressed as:

$$\nu = -\frac{\delta\varepsilon_t}{\delta\varepsilon_a} \tag{1}$$

* Correspondence to: Research Group of Integrated Metallic Nanomaterials Systems, Hamburg University of Technology, Eißendorfer Straße 42 (M), 21073 Hamburg, Germany
E-mail address: shan.shi@tuhh.de (S. Shi).

https://doi.org/10.1016/j.actamat.2025.121393
Received 25 March 2025; Received in revised form 30 July 2025; Accepted 1 August 2025
Available online 9 August 2025

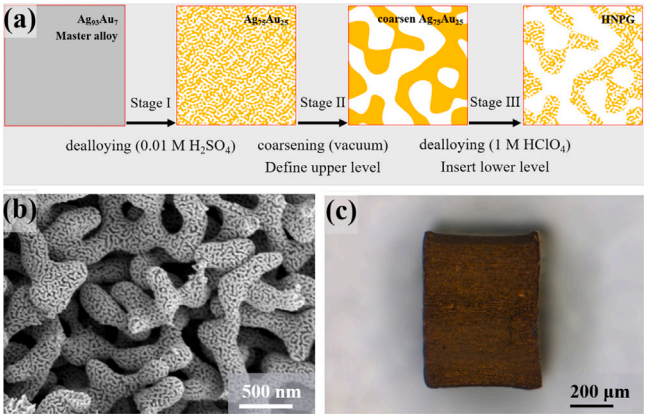

Fig. 1. Preparation process, appearance and microstructure of hierarchical nanoporous gold (HNPG). (a) Scheme describing the synthesis route and structural features of each stage from $Ag_{93}Au_7$ master alloy to nanoporous $Ag_{75}Au_{25}$ (NPSG) alloy and then to HNPG, (b) SEM images showing the fracture surface microstructure of HNPG. The lower level ligaments were embedded in the upper level ligaments to form a hierarchical structure. (c) Optical microscope images of HNPG free from cracks and defects. The dimensions and weight are then measured to obtain the solid volume fraction.

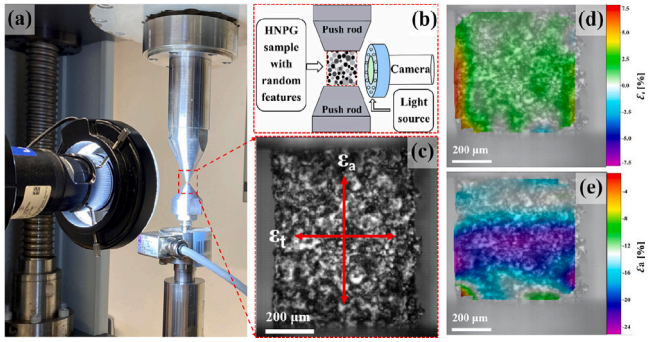

Fig. 2. The digital image correlation (DIC) setup for measuring Poisson's ratio of a HNPG sample during uniaxial macro-compression. (a) Photo of the setup. Left side of the image is a high-precision/high-speed camera and a matching adjustable illumination device. The sample to be tested is placed between the conical push rods of a universal mechanical testing device, which are designed to provide an enhanced illumination on the surface of the sample being tested. (b) Simplified schematic diagram of the setup, illustrating that the random characteristics of the sample surface are created using artificial spray paint to enhance contrast and allow more accurate DIC analysis. (c) A high-resolution image of one HNPG sample under the camera with proper exposure and focus to ensure the accuracy of DIC analysis. ε_t and ε_a represent the transverse and axial strain respectively. Virtual strain gauge maps of (d) ε_t and (e) ε_a when the engineering strain is 10%.

where ε_t denotes transverse strain and ε_a denotes axial strain when a material is stretched or compressed. Indeed, even for non-hierarchical NPG, the studies on Poisson's ratio are quite limited comparable to Young's modulus and yield strength, mainly due to the difficulties in producing high-quality samples and accurate measurements of the transverse strain. In this work, we fabricated crack-free HNPG bulk samples with tunable upper level ligament sizes by a dealloying-coarsening-dealloying method. Using digital image correlation (DIC) and loading/unloading protocols during macroscopic compression, the elastic Poisson's ratio and plastic Poisson's ratio were successfully measured at different stages of engineering strain for HNPG samples with different structure size and density. Moreover, we propose a novel scaling law for the elastic Poisson's ratio of hierarchical nanoscale network materials, and verify it by our experimental results.

2. Experimental procedures

2.1. Master alloy

$Ag_{93}Au_7$ (at.%) master alloy was produced by alloying Au wires (99.95%, Alfa Aesar) and Ag wires (99.99%, Heraeus Metals) through repeated melting and solidification in an arc-melter (MAM-1, Edmund Bühler) under Ar gas atmosphere. Subsequently, the master alloy ingot was sealed in an evacuated quartz tube and homogenized at 850 °C for over 7 days. The ingot was then cold rolled to a 1.2 mm thick plate using a manual rolling mill, using small increments of strain each time to avoid cracking. Finally, the plate was cut into cuboids 0.8 mm × 0.8 mm × 1.2 mm with a diamond wire saw.

2.2. Hierarchical nanoporous gold

The hierarchical nanoporous gold samples were prepared by using the "dealloying-coarsening-dealloying" synthesis protocol in [19]. As illustrated in Fig. 1a, this synthesis method consists of three stages: in Stage I, the samples were electrochemically dealloyed from the $Ag_{93}Au_7$ master alloy to nanoporous $Ag_{75}Au_{25}$ (NPSG) alloy; in Stage II, the NPSG samples were annealed at a given temperature T_a (from 300 °C to 450 °C in this work) for 30 min in vacuum (< 10^{-6} bar, MILA-5000, ULVAC) to form a coarsened porous network structure, which is the upper hierarchical structure; in Stage III, the fine porous or network structure, which is the lower hierarchical level structure, was formed inside the coarsened upper level ligaments through a second dealloying process. During dealloying, a potentiostat (PGSTAT 302N, Metrohm) was used. The scanning electron microscope (SEM) and optical microscope images of one representative sample, as-prepared HNPG, are presented in Fig. 1b and c, respectively.

2.3. Scanning electron microscopy

A scanning electron microscope (FEI Helios Nano Lab G3) equipped with an immersion lens was used to characterize the microstructure of NPSG and HNPG. A working distance of around 4 mm and an accelerating voltage of 2 kV were used. To characterize the internal structure and confirm the structural uniformity, SEM images are taken of the fracture surfaces of the samples. The cross-sectioning was performed by precision cutting of the center of the samples using a scalpel for as-prepared samples. For the cutting of plastically deformed samples, focused ion beam (FIB) milling with gallium source was used to initially fabricate a micropillar with a diameter of 8 μm and a height-to-diameter aspect ratio of 2.5. To avoid excessive damage by the ion beam to the microstructure, the micropillar was milled stepwise, gradually reducing the ion beam current from 5.0 nA to 0.5 nA at an accelerating voltage of 30 kV. To minimize FIB-induced surface artifacts, such as curtaining, a protective platinum layer was deposited on top of the micropillar prior to cross-sectioning, which was subsequently carried out at 30 kV and 0.5 nA. Ligament size, defined as the mean diameter of the ligaments, was determined by measuring the neck of at least 50 ligaments in a single SEM image using ImageJ software (version 1.53k) [22]. The chemical compositions of the NPSG and HNPG samples were determined by means of energy-dispersive X-ray (EDX) analysis. EDX measurements were also performed on the fracture surfaces of the samples with a working distance of around 4 mm and an accelerating voltage of 15 kV.

2.4. Mechanical tests

Uniaxial compression tests were performed using a universal mechanical testing machine (Zwick 1474). The testing machine is equipped with a high-resolution camera (LaVision, Phantom Miro M-series) to capture detailed images during deformation, enabling precise strain measurements based on the high-resolution images. In-situ DIC analysis was performed using professional software (DaVis 8.3.0) to process

and analyze the captured digital images. An engineering strain rate of 10^{-4} /s, a preload of 0.5 N, and unload/reload cycles were applied in all tests. The effective Young's modulus E at a given strain was determined by calculating the secant modulus from the corresponding loading/unloading segment. To obtain high-quality images suitable for the DIC analysis, proper illumination and specific features on the surface of the specimen are essential. In our setup, we constructed a cylindrical push rod, as shown in Fig. 2a and b, to ensure uniform illumination across the samples. Furthermore, a multi-color painting technique using black, white and gray was applied to generate random, high-contrast features, enhancing image quality for accurate strain measurement, as illustrated in Fig. 2c. This approach ensures accurate strain measurements. Virtual strain gauges were positioned on the sample surface in a manner that allowed for the measurement of the axial strain parallel to the loading direction, denoted as ε_a, and transverse strain perpendicular to loading direction, denoted as ε_t (see Fig. 2c–e) [5,23]. Poisson's ratio is measured during both elastic and plastic deformation regimes and is called elastic Poisson's ratio (ν_E) and plastic Poisson's ratios (ν_P), respectively.

3. Scaling laws

For open porous materials with a small solid fraction (φ), their mechanical properties (P) often follow the Gibson–Ashby scaling laws $P = bP_0\varphi^{\beta}$ with b and β constants [24,25] and P_0 denotes the mechanical properties of the massive or local materials. Gibson–Ashby power laws provide a robust foundation for predicting mechanical properties including elastic modulus and strength of low-density cellular solids such as foams and porous materials having connectivity invariable with solid volume fraction [25], while for random porous structure having connectivity varying with solid volume fraction and a percolation threshold (φ_{per}), the following modified Roberts–Garboczi scaling laws were introduced,

$$P_{net} = P_0 C \left(\frac{\varphi_{net} - \varphi_{per}}{1 - \varphi_{per}}\right)^m \tag{2}$$

where C and m are constants.

In a hierarchical nanoscale network material, the overall mechanical response, P_n, is composed of the individual mechanical contributions provided by each hierarchy level, P_j. Analogous to Eq. (2), P_n can be therefore expressed as:

$$P_n = P_0 C^n \prod_{j=1}^{n} \left(\frac{\varphi_j - \varphi_{per}}{1 - \varphi_{per}}\right)^m \tag{3}$$

where n denotes the number of hierarchical levels.

For simplicity, assuming identical solid volume fraction and similar geometry at each hierarchical level (nested network [13,19]), Eq. (3) becomes:

$$P_{net} = P_0 C^n \left(\frac{\varphi_{net}^{1/n} - \varphi_{per}}{1 - \varphi_{per}}\right)^{mn} \tag{4}$$

where P_{net} denotes the mechanical property of a n-level hierarchical network material for $\varphi_{net} \le 2^{-n}$.

It has been reported that Roberts–Garboczi scaling laws can describe fairly well the dependency of both Young's modulus and shear modulus on solid volume fraction for random porous network materials having a percolation threshold [26]. According to equation Eq. (4), the Young's modulus E and shear modulus G of hierarchical random network materials can be written as:

$$E_{net} = C_E^n E_0 \left(\frac{\varphi_{net}^{1/n} - \varphi_{per}}{1 - \varphi_{per}}\right)^{nm_E} \tag{5}$$

$$G_{net} = C_G^n G_0 \left(\frac{\varphi_{net}^{1/n} - \varphi_{per}}{1 - \varphi_{per}}\right)^{nm_G} \tag{6}$$

where C_E and m_E are the characteristic constants for Young's modulus; C_G and m_G are the characteristic constants for shear modulus; E_0 and G_0 denote the Young's modulus and the shear modulus of the solid material, respectively.

For isotropic materials, the above three elastic constants have the following relationship [27]:

$$\nu_E = \frac{E}{2G} - 1. \tag{7}$$

Taking Eq. (5) for E and Eq. (6) for G in Eq. (7), the scaling equation for the elastic Poisson's ratio of a n-level hierarchical network material ($\nu_{E_{net}}$) is derived as:

$$\nu_{E_{net}} = (\nu_{E0} + 1)\left(\frac{C_E}{C_G}\right)^n \left(\frac{\varphi_{net}^{1/n} - \varphi_{per}}{1 - \varphi_{per}}\right)^{n(m_E - m_G)} - 1 \tag{8}$$

where ν_{E0} denotes the elastic Poisson's ratio of the solid material.

Young's modulus

For uni-modal nanoporous structure produced by dealloying, a self-organization process, at low φ_{net}, ligaments with high aspect ratios are prone to disconnection due to the Plateau–Rayleigh instability [3,28,29] and finally form disconnected clusters when φ_{net} decreases to a limit value, namely the critical percolation threshold, φ_{per} = 0.159 [30]. Modified Roberts–Garboczi equations have been introduced to describe the relationship between mechanical properties and solid volume fraction in dealloying-made NPG by Soyarslan et al. [30]. The fitting with simulation results gave $C_E \approx 2.0$ and $m_E \approx 2.5$, which values are also supported by experimental data on NPG with $n = 1$ in literature. These constants remain valid when describing the scaling behavior of Young's modulus in HNPG with $n = 2$ [19]. The scaling law for Young's modulus in hierarchical nanoporous metals with nested network structure and equal solid volume fraction at each hierarchical level takes the form [19]:

$$E_{net} = E_0\, 2^n \left(\frac{\varphi_{net}^{1/n} - \varphi_{per}}{1 - \varphi_{per}}\right)^{5n/2} \tag{9}$$

for $\varphi_{net} \le 2^{-n}$, where n denotes the number of hierarchy levels, E_0 = 79 GPa for Au [31].

Shear modulus

Direct measurements on the shear modulus of NPG are not available in the literature. According to Eq. (7), we estimated the values of G based on the measured ν_E and E of NPG in literature [5,23,32,33,33–35]. By fitting the data using Eq. (6) with n = 1 and taking G_0 = 27 GPa for Au [31], we obtained the characterized constants $C_G \approx 2.0$ and $m_G \approx 2.4$. The fitting curve is shown in Fig. A.1(a). The modified Roberts–Garboczi scaling equation for shear modulus then takes the form:

$$G_{net} = G_0\, 2^n \left(\frac{\varphi_{net}^{1/n} - \varphi_{per}}{1 - \varphi_{per}}\right)^{2.4n} \tag{10}$$

Elastic Poisson's ratio

Taking the characteristic constants for E in Eq. (9) and for G in Eq. (10), thus we have the scaling equation of ν_E as:

$$\nu_{E_{net}} = (\nu_{E0} + 1)\left(\frac{\varphi_{net}^{1/n} - \varphi_{per}}{1 - \varphi_{per}}\right)^{0.1n} - 1 \tag{11}$$

Scaling curves of elastic Poisson's ratio with solid volume fraction for n = 1 and 2 are shown in Fig. A.1b.

4. Results

4.1. Microstructure

The microstructure variation in NPSG and HNPG when adjusting T_a in Stage II are characterized by SEM. Fig. 3a - d shows that the ligament sizes of NPSG samples increase from 60 nm to 180 nm when T_a

Table 1
Structural parameters of hierarchical nanoporous gold (HNPG) samples.

T_a (°C)	φ_{net}	φ_1	φ_2	L_1 (nm)	L_2 (nm)
300	0.146 ± 0.013	0.457 ± 0.021	0.319 ± 0.020	20 ± 2	60 ± 3
350	0.131 ± 0.014	0.402 ± 0.022	0.327 ± 0.019	20 ± 2	100 ± 9
400	0.129 ± 0.020	0.385 ± 0.028	0.336 ± 0.021	20 ± 2	140 ± 11
450	0.126 ± 0.015	0.390 ± 0.035	0.322 ± 0.046	20 ± 2	180 ± 12

Note: T_a, annealing temperature. The data for solid volume fraction and ligaments size take the mean value of at least 10 samples. φ_1 and φ_2 denote solid volume fraction of the lower and upper level hierarchical structures, respectively. φ_{net} denotes net or total solid volume fraction of HNPG, where $\varphi_{net} = \varphi_1 \times \varphi_2$.

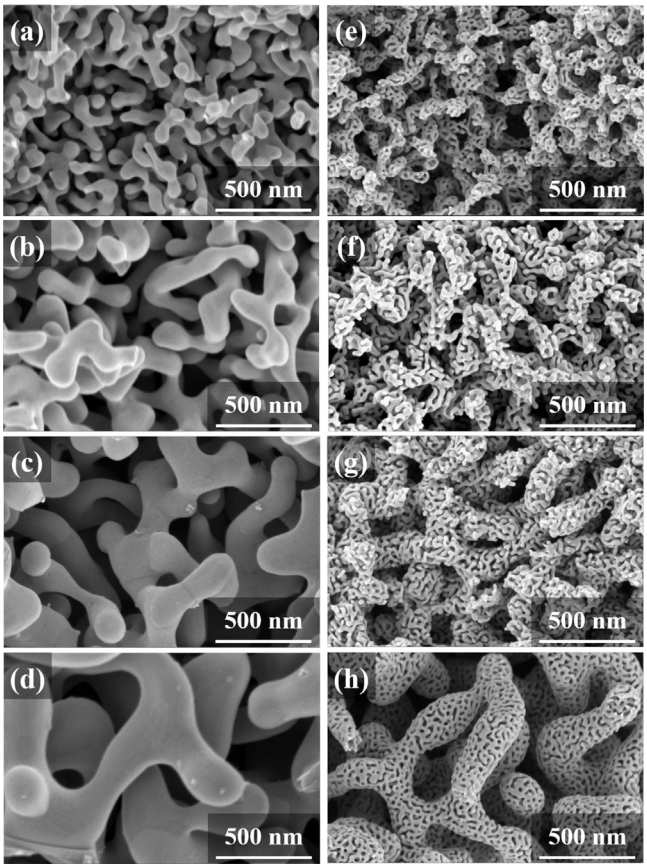

Fig. 3. Microstructure of NPSG alloy and HNPG samples at different annealing temperatures. (a–d) SEM images of NPSG alloy annealed at 300 °C, 350 °C, 400 °C and 450 °C, respectively, showing ligament sizes of 60 nm, 100 nm, 140 nm and 180 nm. (e–h) SEM images of the HNPG samples dealloyed out of NPSG alloy samples in (a–d), showing the same lower level ligament size (L_1) of 20 nm, while the upper level ligament size (L_2) retain the original ligament size of the corresponding nanoporous $Ag_{75}Au_{25}$ alloys.

increases from 300 °C to 450 °C. Fig. 3e–h shows that the upper ligament sizes (L_2) of HNPG also increase with increasing T_a. Clearly, the values of L_2 in HNPG are similar to the ligament sizes of corresponding NPSG, increasing from 60 nm to 180 nm as T_a increases from 300 °C to 450 °C. By contrast, all HNPG samples show the same ligament size of $L_1 = 20$ nm at the lower hierarchy level irrespective of T_a, attributing to the same dealloying conditions at Stage III. The mean values of L_1 and L_2 that obtained by measuring at least 10 samples for each synthesis condition are listed in Table 1. EDX measurements indicate that the residual Ag contents in NPSG and HNPG are 75 ± 1 at.% and less than 2 at.%, respectively.

Table 1 also includes the information on solid volume fraction of the investigated NPSG and HNPG samples. The net solid volume fraction (φ_{net}), or relative density, of as-prepared NPSG and HNPG samples was estimated by measuring samples' mass and volume. Under the assumption of invariable solid volume fraction for the upper level hierarchical structure during annealing and in Stage III, the solid volume fraction of structure at upper hierarchical level (φ_2) is supposed to equal to φ_{net} of corresponding NPSG. The values and error bars for φ_{net} and φ_2 listed in Table 1 are obtained by measuring at least 10 samples. The solid volume fraction of structure at lower hierarchical level (φ_1), is then estimated by:

$$\varphi_1 = \frac{\varphi_{net}}{\varphi_2} \tag{12}$$

It is observed that HNPG samples with the smallest $L_2 = 60$ nm show the highest $\varphi_{net} = 0.146$, while HNPG samples with larger L_2 show φ_{net} in the range of 0.126 to 0.131. This is consistent with the trend for φ_2 of HNPG and φ_{net} of NPSG. That is mainly due to the relatively small size of upper level L_2. During the dealloying process, nanoporous gold can densify near its external surface which has been reported by previously published work [36]. This induced a higher φ_1 and then φ_{net} in $L_2 = 60$ nm sample for all the lower level ligaments are relatively more closer to the external surface due to the smaller upper level ligaments' size compared to other samples.

4.2. Mechanical properties

The uniaxial compression tests were carried out on millimeter sized HNPG samples by using a conventional mechanical testing device as shown in Fig. 2a. Mechanical properties, including Young's modulus and both elastic and plastic Poisson's ratio, were obtained by measuring more than 40 crack-free HNPG samples. All samples have a similar lower level ligament size of $L_1 = 20$ nm. The mean values for L_2 (60 nm–180 nm), φ_{net} (0.126–0.146), φ_1 (0.319–0.336) and φ_2 (0.385–0.457) varying with annealing temperature are listed in Table 1. All samples were compressed to an engineering strain exceeding 60%. Note that only the Young's modulus and Poisson's ratio in the deformation stage of the first 35% ε_{eng} was further analyzed and discussed subsequently.

Fig. 4a shows the engineering stress–strain curves featuring loading/unloading segments of four representative HNPG samples with L_2 varying from 60 nm to 180 nm but nearly the same φ_{net} (0.142). It shows that all samples can undergo large plastic strains over 60% without cracks or failure. The flow stress increases continuously with the increasing engineering strain for all four samples, due to the effects of strain hardening and densification. The variation of E, ν_E and ν_P during compression are shown in Fig. 4b–d, respectively. Fig. 4b shows that E increases with ε_{eng} for all HNPG samples due to the densification-induced increase in solid volume fraction. It is also observed that, despite having nearly the same φ_{net}, HNPG with the smallest L_2 shows a slightly higher elastic modulus value than the other three samples. This might be explained by a greater reduction in connectivity during the annealing stage for the other three samples with larger L_2 [9,29].

Fig. 4c and d show ν_E and ν_P versus ε_{eng}, respectively. Different from the relationship between E and ε_{eng}, both ν_E and ν_P remain nearly constant during the entire compression, irrespective of L_2. There is a slight increase in ν_E with strain even until a compressive strain of ε_{eng} = 60%; there is a slight decrease in ν_P with strain at the small strain (<

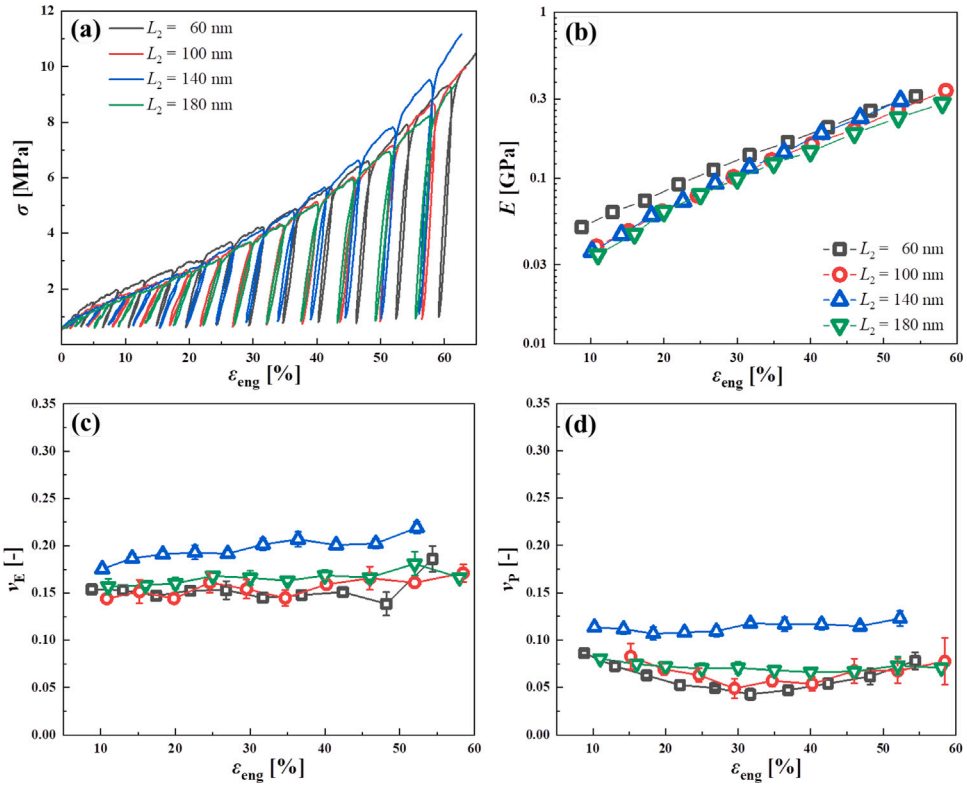

Fig. 4. Results of uniaxial loading/unloading compression test of 4 representative HNPG samples with different L_2 varying from 60 nm to 180 nm and approximate initial solid volume fractions of 0.144, 0.142, 0.141 and 0.142, respectively. (a) Engineering stress–strain curves (σ - ε_{eng}). The zoomed image shows a loading/unloading segment, (b) The log-linear plot of Young's modulus E as a function of engineering strain ε_{eng}, (c) Elastic Poisson's ratio (ν_E) as a function of engineering strain (ε_{eng}) and (d) Plastic Poisson's ratio (ν_P) as a function of ε_{eng}. The error bars represent the standard deviation, which are the max and min values of measured ν_E and ν_P during each elastic and plastic deformation stage.

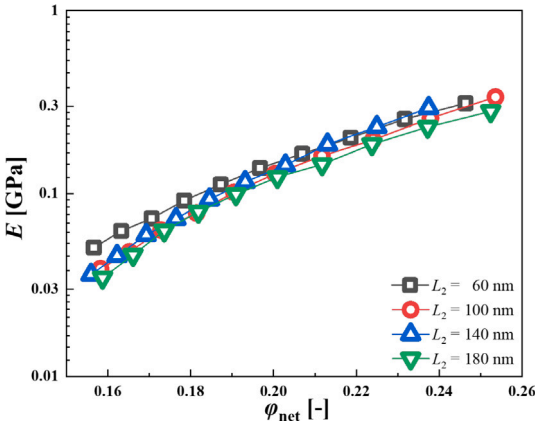

Fig. 5. The log-linear plot of Young's modulus (E) as a function of the network solid volume fraction (φ_{net}) of HNPG at different compressive strains. The four HNPG samples have an approximately same initial φ_{net} = 0.142 and L_2 vary from 60 nm to 180 nm.

30%) and then an increase in ν_P with strain at the large strain regime (> 30%). This indicates that the deformation changed solid volume fraction and morphology/topology, but the change of these parameters have different influences on E and ν.

Fig. 5 plots E versus φ_{net} for the four HNPG samples from Fig. 4. The values of φ_{net} of all these four HNPG samples increase to around 0.26 as ε_{eng} increases to 60%. These deformed HNPG samples show an increase of E with increasing φ_{net}. In addition, we observed that the four E versus φ_{net} curves gradually converge, indicating E becomes independent of L_2 in the highly deformed state. This suggests that the new connections resulting from the compression process effectively compensate for the different reduction in connectivity or disconnections that occur during the annealing stage of synthesis.

Fig. 6 presents the relationship between ν_E and φ_{net} for HNPG samples with distinct L_2 values under a compressive strain of up to 35%. The results for the four samples from Fig. 4, one for each L_2 (60 nm, 100 nm, 140 nm and 180 nm), are indicated by the open symbols in Fig. 6a–d, respectively. The plots of ν_E in response to engineering strain are shown in Fig. A.2a - d. It is interesting that even though a large compression deformation leads to an increase in φ_{net}, it has no significant effect on the ν_E across all the samples. ν_E shows very slight increase, almost invariable, during compression, although both the solid volume fraction and the network connectivity increase substantially during deformation. Some possible underlying causes of this unexpected observation are included in our Discussion Section.

In addition to these four samples, at least additional 9 samples for each L_2 were measured. The yellow shaded areas in Fig. 6a - d represent the average results obtained from at least 10 HNPG samples for each L_2. These HNPG samples show φ_{net} in the range of 0.14–0.22 and ν_E in the range of 0.11–0.21. Focusing on low φ_{net} regimes (φ_{net} = 0.14–0.16) or in other words small plastic deformation regions, all HNPG samples have ν_E close to 0.15, except for a slightly higher ν_E observed for HNPG with L_2 = 140 nm in Fig. 6c. This observation agrees overall with the size independence of ν_E in non-hierarchical nanoporous metals [5]. The deviations between samples with identical or different L_2, especially for samples with relatively larger L_2, might be attributed to the variations in connectivity resulting from the coarsening and shrinking processes in the synthesis.

Fig. 7 shows the effect of L_2 on the relationship between ν_P and φ_{net}. Same to Fig. 4 and Fig. 5, results from the four HNPG samples with different L_2 and an approximately identical φ are presented here. It shows in the regime of φ_{net} = 0.15 - 0.22, ν_P varies from 0.05 to 0.12. Similar to the effect of L_2 on ν_E shown in Fig. 6, the HNPG sample with

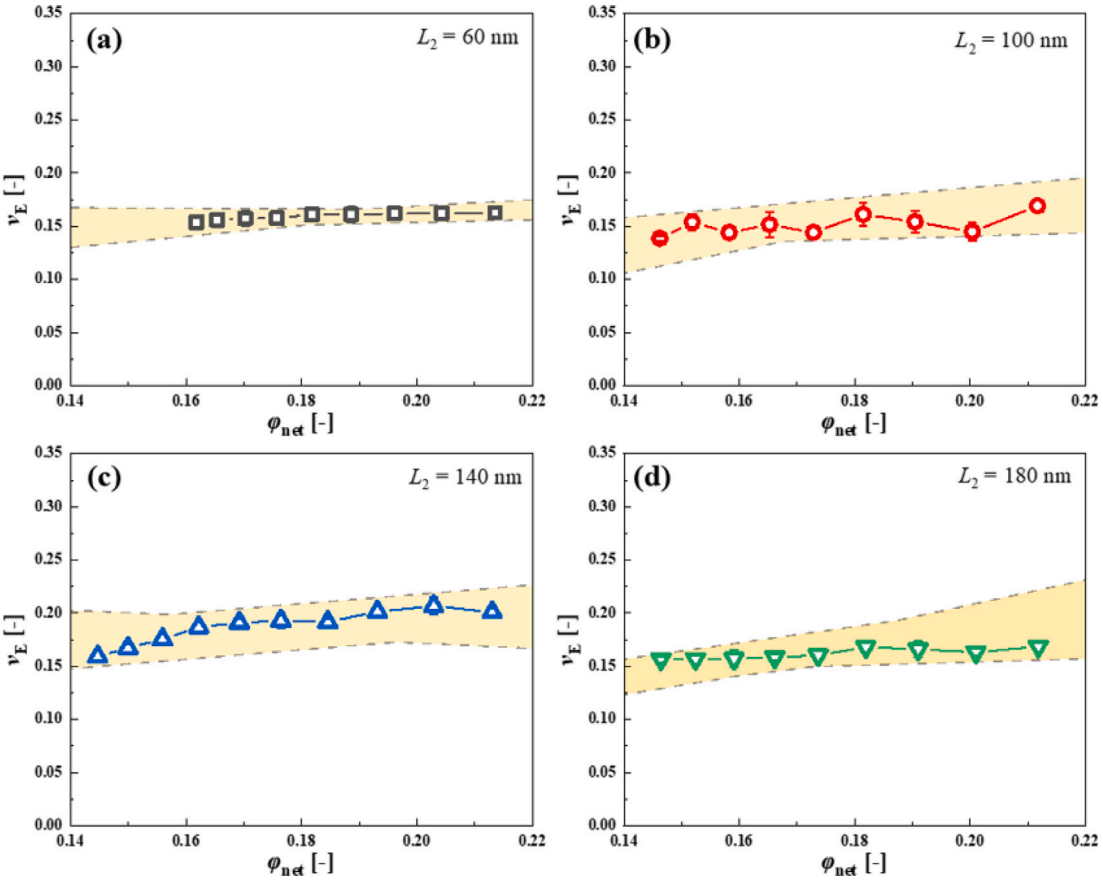

Fig. 6. The variations in the ν_E of HNPG with different L_2 as a function of φ_{net} evolution are presented. (a), (b), (c) and (d) ν_E for HNPG samples with L_2 ranging from 60 nm to 180 nm. The yellow-shaded region in each figure represents the spread of ν_E for at least 10 samples, with the upper and lower boundaries defined by the maximum and minimum values at the corresponding φ_{net}. Additionally, the ν_E of a representative sample is included within each shaded region. The error bars represent the standard deviation, which are the max and min values of measured ν_E during each elastic deformation stage.

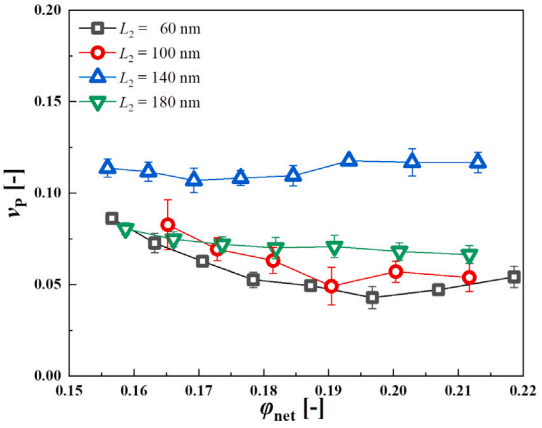

Fig. 7. The variations of the ν_P of 4 representative HNPG samples with different L_2, ranging from 60 nm to 180 nm, and approximate initial φ_{net}, are shown as a function of φ_{net}. The error bars represent the standard deviation, which are the max and min values of measured ν_P during each plastic deformation stage.

L_2 = 140 nm shows a slightly larger ν_P than the other three samples, irrespective of φ_{net}. It is also observed that ν_P of each sample shows much larger fluctuation as φ_{net} varies from 0.15 to 0.22, especially for HNPG with smaller L_2. This is not unexpected, as even non-hierarchical NPG has exhibited larger variations in ν_P with engineering strain, as reported in [5].

5. Discussion

5.1. Impact of upper level ligament size

Based on the mechanical measurements for HNPG with L_2 and similar L_1, the impact of upper level ligament size on the Poisson's ratio, Young's modulus and effective solid volume fraction (φ_{eff}) were analyzed and illustrated in Fig. 8. The Poisson's ratio and Young's modulus at ε_{eng} = 10% are taken and plotted against L_2. Each data point in Fig. 8 means an average value of at least 10 HNPG samples, and the upper and lower limits of each error bar are the maximum and minimum values, respectively.

As shown in Fig. 8a, in the investigated regime L_2 from 60 nm to 180 nm, ν_E does not show obvious upper level size dependence. The average values of ν_E remain close to 0.15. This trend is very consistent with the conclusion of Lührs et al. who observed size independent elastic Poisson's ratio through investigating NPG with the same φ_{net} = 0.25 and varying ligament size from 50 nm to 180 nm [5]. However, in HNPG, we can see relatively large error bars for ν_E especially at low L_2 cases. This deviation can be caused by the different φ_{net} among samples, consistent with the error bars for solid volume fraction at each synthesis variable in Table 1. Although it has been demonstrated that HNPG shows improved specific stiffness and specific strength compared to NPG, the absolute stiffness and strength of HNPG are smaller than that of NPG. This is due to the fact that the HNPG samples explored in this work have a much lower relative density, which is only half of the density of the monolithic NPG samples studied by Lührs et al. [5]. Moreover, practically, the smaller sample sizes of HNPG may increase the possibility of different plastic deformations caused by the pressure

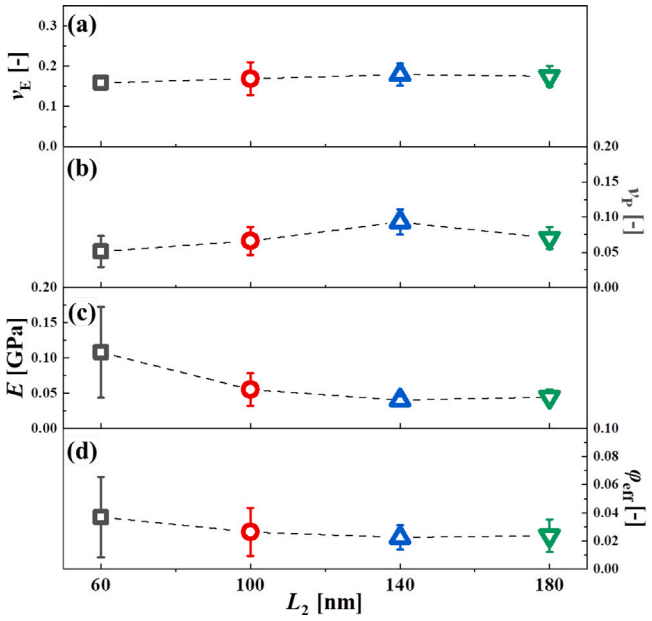

Fig. 8. Average values of ν_E, ν_P, E and φ_{eff} at 10% ε_{eng} as a function of L_2. (a) ν_E, (b) ν_P, (c) E and (d) φ_{eff}. φ_{eff} is calculated from the E using Eq. (13). Each data point represents the average value of at least 10 HNPG samples, with an error bar showing the max and min values.

from sample holders during both dealloying and handling of the samples afterwards, therefore leading to a different degree of shrinkage or plastic deformation and then different solid volume fractions among samples. In addition, such variation in ν_E for HNPG with a small L_2 might also be caused by the variation of connectivity among samples.

Similar to the effect of L_2 on ν_E in Fig. 8a, Fig. 8b shows ν_P stays at around 0.075, half of ν_E. The similar ν_P can be attributed to the similar lower level ligament size, which typically plays a significant role in the plastic behaviors, in this case, transverse strain during plastic deformation in compression. We suppose that the slight difference among samples is originated from the difference in network connectivity and solid volume fraction.

In addition, to explore the role of L_1 on ν_P, L_1 was adjusted to < 20 nm and 40 nm, respectively, while keeping L_2 = 140 nm (Fig. A.3). It can be seen that ν_P for the two new sets of samples are within the range of 0.05–0.10 (Fig. A.4), consistent with the values for HNPG with L_1 = 20 nm. In contrast to the clear size effect observed in NPG by Lührs et al. [5,23], there is no obvious trend between L_1 and ν_P in the HNPG samples studied here. This is reasonable, as tuning L_1 introduces additional variations in chemical composition and topology. HNPG samples with L_1 < 20 nm contain a high residual silver content up to 16at.%, while coarsening processes for increasing L_1 up to 40 nm and a reduced L_2/L_1 ratio,both of which contribute to connectivity variation [19,29,37]. The effects of ligament size and L_2/L_1 ratio on the connectivity are further discussed in the following paragraph. Our observations are consistent with the structure-insensitive ν_P phenomenon in NPG reported by Liu et al. [38]. In addition to ligament size, other factors such as network connectivity, residual Ag distribution and solid fraction all may vary significantly during coarsening, and these parameters may influence ν_P simultaneously. It is challenging to isolate the effect of a single factor. More dedicated and systematic experiments are needed to decouple the contributions of these individual parameters.

The variation of E with L_2 is shown in Fig. 8c. It is observed that there is a large difference in E for HNPG samples with L_2 = 60 nm. This is very likely is due to the very small ratio between L_2 and L_1. The small L_2/L_1 = 3 means a very limited number of lower level ligaments within one upper level ligament, in other words, a non-representative volume element for the network at the lower hierarchical level. Ligament structures formed from non-representative volume elements are subjected to considerable scatter in connectivity, which in turn causes variation of the mechanical properties such as Young's modulus and yield stress [37]. Moreover, small L_2/L_1 value may lead to more dangling lower level ligaments at the surface of upper level ligaments. These dangling lower level ligaments do not contribute to load bearing, resulting in a reduction in connectivity of the structure at the lower hierarchy level and hence reduction in Young's modulus with a decrease in L_2. The effect of L_2 on the connectivity of the lower level network in HNPG is similar to the effect of the tested pillar diameter on the mechanical response of NPG with a fixed ligament size observed by Wu et al. [37]. Wu et al. found the representative volume element of NPG corresponds to a pillar-ligament size ratio of 20, below which value, Young's modulus decreases with increasing number of dangling ligaments at the surface of the tested pillar and eventually becomes stochastic when a pillar-ligament size ratio falls below 10 accompanied by non-uniform deformation and failure. This supports our observation that there is a large variation of E even though they have the same L_2 = 60 nm, while with increasing L_2 or L_2/L_1, the scattering of E among samples becomes smaller and eventually becomes negligible at L_2/L_1 > 7.

In addition to the effect of L_2 (in fact, L_2/L_1) on the connectivity of the network at the lower hierarchical level, L_2 plays a role on the connectivity of the network at the upper hierarchical level. According to the simulation by Li et al. [29] and evidence by experiments on NPG [6], there exists a connectivity loss during coarsening for low solid volume fraction NPG structures. This indicates a reduction in the connectivity of the network at the upper hierarchical level with increasing L_2, hence a lower stiffness of the upper level structure at greater L_2. To sum up, the effect of L_2 on the network connectivity at both lower and upper hierarchical levels results in the different stiffness in HNPG with a fixed L_2.

As an indication of the total connectivity of entire network, we estimated the effective solid volume fraction (φ_{eff}), a concept introduced by Jin et al. [4],

$$\varphi_{eff} = \left(\frac{E}{E_0}\right)^{0.5} \tag{13}$$

where E takes the measured Young's modulus of HNPG sample and for E_0 takes the Young's modulus of bulk Au, 79 GPa [31]. Fig. 8d shows a large variation of φ_{eff} from 0.010 to 0.065 for HNPG samples with the same L_2 = 60 nm. With the increase of L_2, in other words, L_2/L_1, the scattering of φ_{eff} shows exactly the same trend as the scattering of E for each L_2. At L_2/L_1 >7, E and φ_{eff} becomes stable at around 0.05 GPa and 0.025, respectively. The upper level size dependence of Young's modulus also agrees well with the previous work on HNPG by Shi et al. [19]. Furthermore, it appears that the network connectivity has a different or greater effect on E compared to its effect on ν_E and ν_P.

5.2. Impact of solid volume fraction

Scaling behavior of elastic Poisson's ratio

Fig. 9 shows the scaling behaviors of ν_E in response to φ_{net} for NPG (n = 1) and HNPG (n = 2), respectively. The experimental data for NPG from literature and for HNPG from this work, and several scaling laws are plotted together for comparison. The scaling laws presented include Gibson–Ashby's equation [25], Soyarslan's equation [30] and our Eq. (11). It clearly shows that experimental results of both NPG and HNPG fit well with the prediction of our scaling law. The proposed scaling law describes the relationship well between ν_E and φ_{net} for nanoporous metals (n = 1) in general, while the other scaling curves (see gray dot line and blue dash line in Fig. 9) overestimate ν_E at low solid fractions particularly when approaching φ_{per}. Most importantly, our scaling equation addresses how ν_E scales with φ_{net} for hierarchical structure (n > 1). This resolves an important knowledge gap

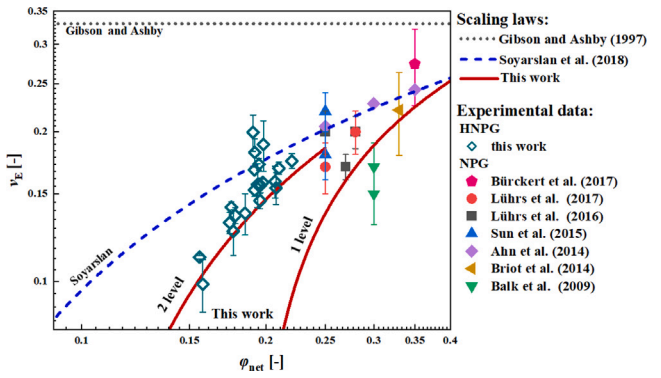

Fig. 9. Scaling behavior of ν_E with respect to φ_{net} of nanoporous gold with different numbers of hierarchical levels. Close symbols: Literature experimental data, which were obtained from microscale NPG samples using compression testing [32,33], tensile testing [33,34], and ultrasonic testing techniques [39] and from compression tests on millimeter-sized NPG samples [5,23,35]. Open symbols: experimental data from compression tests on millimeter-sized HNPG samples in this work. Gray dot line: Gibson–Ashby equation, $\nu_E = 0.33$ [25]. Blue dash line: Soyarslan's law, $\nu_E = D_1 \ln\varphi_{net} + D_2$, where $D_1 = 0.116$, $D_2 = 0.363$ [30]. Red solid lines: Scaling law proposed in this work by Eq. (11), with $n = 1$ and $n = 2$, respectively. The error bars for HNPG take the max and min values of measured ν_E for each sample; the error bars for NPG are taken directly from literature.

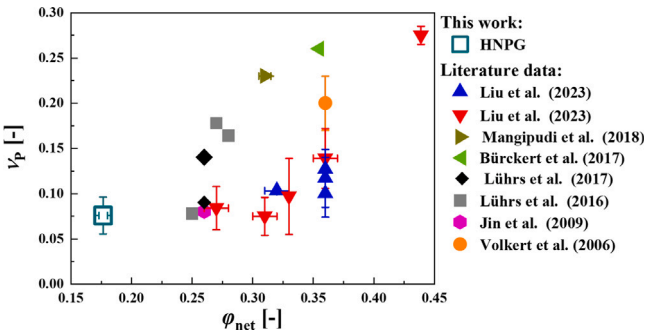

Fig. 10. ν_P of HNPG as a function of φ_{net}, compared to ν_P of NPG from various sources [5,8,23,35,48–50] in literature. The error bars for HNPG were obtained from at least 5 samples at ε_{eng} around 10%, indicating the max and min measured values, while the error bars for NPG samples are taken directly from literature.

in understanding the fundamental structure–mechanical properties in hierarchical nanoscale network materials.

While the present work focuses on the relationship between Poisson's ratio and the overall solid fraction in HNPG, it is recognized that topological features — particularly connectivity — can influence Poisson's ratio to some extent. Prior studies have demonstrated that connectivity plays a critical role in governing mechanical stiffness [9]. This influence may be especially pronounced in coarsened, low-density nanoporous metals, regardless of the presence of hierarchy. Future investigations that incorporate 3D reconstruction [40,41] and quantitative topological analysis [21,42–44] will be invaluable for refining current scaling laws and extending their applicability across a broader class of hierarchical nanoscale network materials.

It needs to emphasize that scaling equation for elastic Poisson's ratio (Eq. (8)) is derived under the assumption of isotropic structure at each hierarchical level. Consequently, it cannot be directly applied to anisotropic structures, such as unidirectional or periodic, architected networks, which typically exhibit orientation-dependent and even freely tunable mechanical properties [8,16,45–47]. However, the theoretical framework may still be applicable to a broader class of random nanoscale network structures beyond dealloying-made spinodal-like structures and leveled-wave structures. Moreover, the conceptual basis of this theory may provide a foundation for future efforts aimed at modeling the mechanical behavior of anisotropic nanoscale network structures.

Comparison of plastic Poisson's ratio between HNPG and NPG

Fig. 10 shows ν_P versus φ_{net} of HNPG at $\varepsilon_{eng} = 10\%$. The results for NPG from literature work are also presented for comparison [5,8,23,35,48–50]. It shows that there exists a large scattering of ν_P at a given solid volume fraction particularly for NPG. This is not unreasonable because of the varied testing methods and/or different sample conditions (e.g., geometry, plastic deformation, and structure size). It is obvious that ν_P shows an overall decrease trend as φ_{net} decreases. In practice, monolithic NPG samples typically have a solid volume fraction more than 0.2 and ν_P>0.075. Therefore, it is remarkable that our hierarchical nanoporous metals can reach not only much lower solid volume fraction (0.11) but also lower ν_P than widely studied unimodal nanoporous metals, providing more opportunities in materials design.

ν_P is commonly regarded as a key parameter influencing the hardness-to-yield strength ratio, $f = H/\sigma_y$, in cellular materials. For NPG, different f values ranging from 1.0 to 3.0 have been reported in the literature [3,4,38,50,51]. According to the widely accepted empirical Shaw–Sata relation for porous materials [52], a ν_P of 0.075 for our HNPG corresponds to $f = 2.0$. In contrast, simulations by Miller [53] suggest that for porous materials with a low-to-moderate ν_P, indentation hardness is largely insensitive to ν_P and approximates the yield strength, implying $f \approx 1.0$, but deviations from this unity value may be caused by other factors such as strain hardening. Consistent with Miller's simulation, recent experimental work by Liu et al. [38] on various NPG systems has shown that when the solid volume fraction is below 0.3, f is governed mainly by the strain hardening rate, θ, rather than by ν_P. All HNPG samples investigated in this study exhibit pronounced strain hardening, supporting the use of Liu's equation: $f = 1.33 + 0.11\theta/\sigma_y$ [38]. Using this equation, we take σ_y and θ determined at $\varepsilon \approx 0.1$ for HNPG samples with $L_1 = 20$ nm and $L_2 = 60 - 180$ nm, obtaining f values between 1.76 and 1.92. The deviation of f from unity is anticipated in HNPG as a consequence of strain hardening.

5.3. Evolution of mechanical properties during compressive deformation

For NPG, it is well understood that the elastic modulus increases with compressive strain because of densification-induced increase in the solid volume fraction and the formation of new connections between ligaments, leading to a significant increase in the effective solid volume fraction [4]. For HNPG in this work, Fig. 4 exhibits similar evolution of Young's modulus with strain during compression, which also agrees very well with the previous observation by Shi et al. [19]. Remarkably, we found that elastic Poisson's ratio shows almost no changes even after a large plastic deformation, which means after a substantial increase in the actual solid volume fraction due to densification. This observation does not follow the scaling equations between ν_E and φ_{net} in Fig. 9. The trend is similar to Gibson–Ashby model's calculation but ν_E of our deformed HNPG is much smaller than $\nu_E = 0.33$ from Gibson–Ashby [25]. It is reasonable that the scaling behaviors for non-deformed samples cannot apply for deformed samples because of obvious microstructure variation during compression.

For NPG, opposite trends of ν_E-strain relationships were observed in different strain regimes: a clear decrease trend with strain by Bürckert et al. [35] vs an increase trend by Lührs et al. [5]. The less obvious variation of ν_E with compressive strain in our HNPG may relate to the much lower actual φ_{net}, because HNPG is nearly two times lighter than NPG investigated in literature. φ_{net} of NPG usually starts at around 0.25 and raises to 0.40 after 30% compressive deformation, while for HNPG, the φ_{net} usually varies from 0.12 to 0.25, almost no overlap with NPG. It is reported that compressive deformation on HNPG causes different microstructure variation at upper and lower hierarchical level: more severe change, in other words greater plastic deformation and densification, at the upper level structure compared to lower level

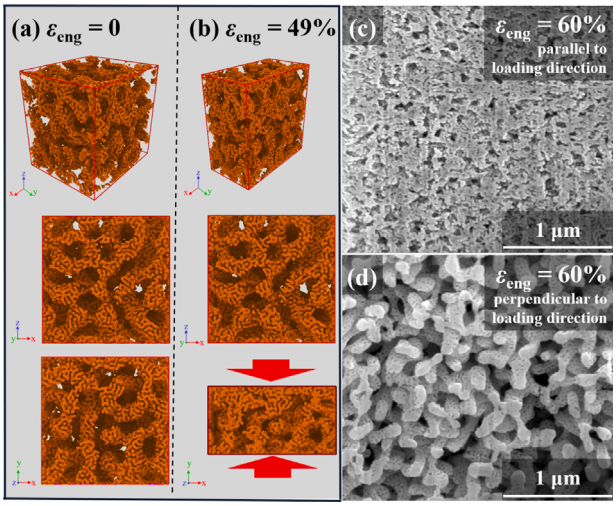

Fig. 11. Microstructure evolution during compression. Molecular dynamics (MD) simulated microstructure of virtual HNPG at a compressive strain of (a) $\varepsilon_{eng} = 0$ and (b) ε_{eng} =49% [19], Top: a three-dimensional overview, middle: cross section perpendicular to the compression direction, bottom cross-section parallel to the compression direction. The loading direction is indicated by red arrows. Reproduced with permission from Shi et al. [19]. Copyright (2021) by American Association for the Advancement of Science. SEM images of the cross sections (c) parallel and (d) perpendicular to the compression direction of HNPG samples at $\varepsilon_{eng} = 60\%$.

structure [19]. Bürckert et al. explained the decrease of ν_E with strain in NPG by the progressive increasing number of yielded ligaments, which therefore makes a limited contribution to the lateral elastic deformation of the sample. This can be the case at the lower level structure in HNPG. The clear increase in the elastic Poisson's ratio with strain observed by Lührs et al. is at significantly large compressive strain, which leads to a much greater solid volume fraction, larger degree of yielding and different distribution in orientation and configuration of the ligaments. These phenomena dominantly occur at the upper level structure in HNPG. Due to the different yielding degree and structure change at upper and lower hierarchy levels during compression, it is also not appropriate to apply one of the conclusions from uni-modal NPG directly to HNPG, as non-uniform microstructure evolution at different hierarchical levels.

In addition, we suspect that Poisson's ratio is dominated by the cross sectional structure perpendicular to the loading direction. This is well supported by the cross sectional images in parallel and perpendicular to the loading directions of real samples in this work and virtual samples taken from Shi et al. [19]. Both the molecular dynamics (MD) simulations on virtual HNPG (Fig. 11 a–b) and the SEM images on real HNPG (Fig. 11 c–d) demonstrated that the cross section in perpendicular to the loading direction shows almost unchanged morphology during compression, while the cross section in parallel to the loading direction shows a clear densification at the upper hierarchical level.

6. Conclusion

This study investigated the elastic and plastic Poisson's ratios in hierarchical nanoporous gold using an in-situ digital image correlation technique. Crack-free monolithic HNPG samples with two well-defined length scales and a nested network structure were fabricated through a dealloying–annealing–dealloying process.

Remarkably, a novel scaling law was introduced to describe the relationship between elastic Poisson's ratio and solid volume fraction in hierarchical nanoscale network materials, which was validated experimentally. By adjusting the annealing temperature during synthesis, the ligament size at the upper hierarchical level was tuned from 60 nm to 180 nm, while the ligament size at the lower hierarchical level remained constant at 20 nm. The results revealed that hierarchical nanoporous gold exhibits negligible dependency of elastic and plastic Poisson's ratios on the upper level ligament size. In contrast to NPG, both Poisson's ratios of HNPG remained nearly unchanged during compression, regardless of upper level ligament size.

This work enables the understanding of the relationships between structural parameters—such as structural hierarchy, structure size, solid fraction—and Poisson's ratios (both elastic and plastic), filling a knowledge gap in the mechanics of hierarchical network nanomaterials. Moreover, these findings can provide a foundation for designing and optimizing materials with tailored mechanical properties. The insights gained may pave the way for developing lightweight, strong materials, opening new opportunities for applications in aerospace engineering, automotive design, and other fields where Poisson's ratios are crucial.

CRediT authorship contribution statement

Haonan Sun: Writing – original draft, Methodology, Investigation, Conceptualization. **Lukas Lührs:** Writing – review & editing, Supervision, Software. **Wei-Che Chang:** Investigation. **Shan Shi:** Writing – review & editing, Supervision, Conceptualization.

Declaration of competing interest

The authors declare that they have no known competing financial interests or personal relationships that could have appeared to influence the work reported in this paper.

Acknowledgment

The authors acknowledge the support by the Deutsche Forschungsgemeinschaft (DFG), Germany, Germany within the Collaborative Research Centre CRC 986 "Tailor-Made Multi-Scale Materials Systems" (Project No. 192346071).

Appendix. Sample appendix section

Fig. A.1 shows the scaling behaviors for shear modulus G and elastic Poisson's ratio ν_E in nanoporous gold with one and two hierarchical levels. We estimated G from experimental E and ν_E of NPG in literature according to Eq. (7) and fitted them with Eq. (6). Then we received $C_G = 2.0 \pm 0.7$ and $m_G = 2.4 \pm 0.4$, or in other words the scaling equation of G for hierarchical nanoscale network materials, Eq. (10). We plotted the scaling curve of G for $n = 2$, and compared it with our experimentally estimated G for HNPG in this work. It shows that the trend for experimental G fits well with the prediction by our scaling equation, but all the experimental data are slightly lower than the predicted values. This phenomenon can be explained by: (1) the scaling law is derived under the assumption of equal solid fraction at each hierarchical level while the real HNPG samples in this study in fact have different solid fractions at two hierarchical levels; and (2) there is connectivity loss during dealloying and coarsening in experimental HNPG samples compared with the leveled-wave structure in Soyarslan's simulation or as-prepared NPG samples in the literature which we use to fit the constants in Eq. (6). Fig. A.1b shows the prediction on ν_E by our scaling equation, Eq. (11), which is obtained by taking (C_G = 2.0, m_G = 2.4) and (C_E = 2.0 and m_E = 2.5 [30]) into Eq. (8). The comparison between prediction and experiments on ν_E for NPG and HNPG are discussed in the main text.

Fig. A.2a–d show the variations of the elastic Poisson's ratio (ν_E) with the engineering strain (ε_{eng}) for HNPG samples with different upper level ligament sizes (L_2). The yellow area in each sub-figure represents the results from at least 10 samples, with results from a representative sample marked as open symbols. It shows that ν_E of all HNPG is around 0.15 at $\varepsilon_{eng} < 35\%$, regardless of L_2.

Fig. A.3 shows the SEM images of hierarchical nanoporous gold (HNPG) with a fixed upper level ligament size L_2 = 140 nm and different lower level ligament size L_1 of < 20 nm, 20 nm and 40 nm, respectively. L_1 is adjusted by changing the dealloying conditions in Stage III. HNPG with $L_1 < 20$ nm in Fig. A.3a is fabricated by applying

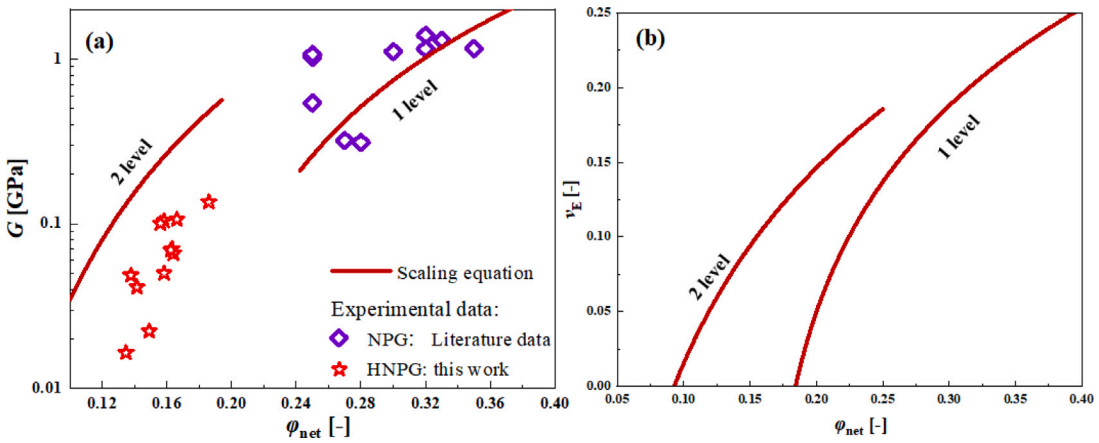

Fig. A.1. Scaling behaviors of shear modulus (G) and elastic Poisson's ratio (ν_E) with solid fraction (φ_{net}) of nanoporous gold with different numbers (n) of hierarchical levels. (a) G versus φ_{net} for $n = 1 - 2$. (b) ν_E versus φ_{net} for $n = 1 - 2$. Open purple rhombuses: G is estimated from experimental E and ν_E of NPG in literature. Open red stars: G is estimated from experimental E and ν_E of HNPG in this work. Red solid lines in (a): Eq. (10). Red solid lines in (b): Eq. (11).

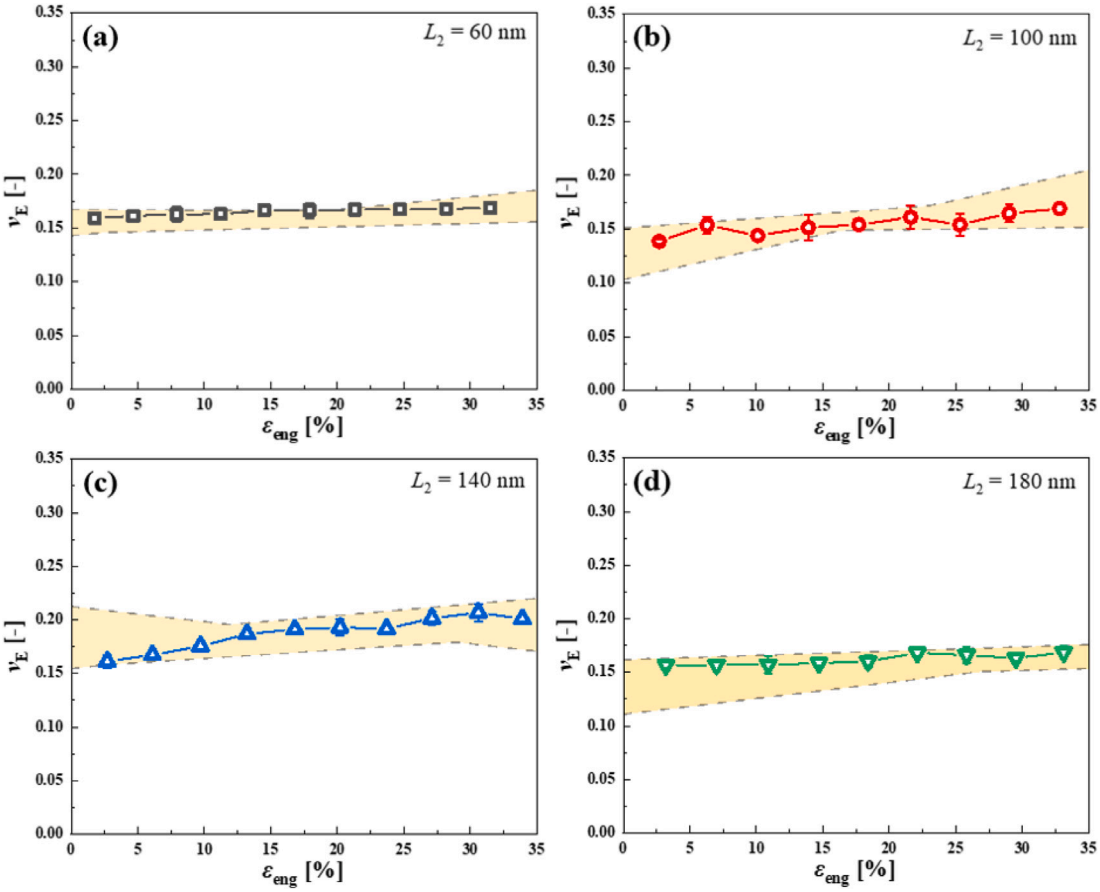

Fig. A.2. The variation of the elastic Poisson's ratio ν_E during compression. (a), (b), (c) and (d) ν_E versus engineering strain ε_{eng} for HNPG samples with L_2 sizes ranging from 60 nm to 180 nm. The yellow-shaded region in each figure represents the spread of ν_E for at least 10 samples, with the upper and lower boundaries defined by the maximum and minimum values at the corresponding ε_{eng}. Additionally, the ν_E of a representative sample is marked as open symbols within each shaded region. The error bars on open symbols represent the standard deviation, which are the max and min values of measured ν_E during each elastic deformation stage.

a constant dealloying potential at E_1 = 1.4 V for 3600 s and then at E_2 = 1.0 V (vs. SHE) for 1800 s in Stage III; HNPG with L_1 = 40 nm in Fig. A.3c is fabricated by applying additional 60 CV cycles on HNPG with L_1 = 20 nm (Fig. A.3b, same to Fig. 3g). A relatively high residual Ag content of around 16 at.% is observed in HNPG with L_1 < 20 nm in contrast to < 2 at.% in HNPG with L_1 = 20 nm and 40 nm.

Fig. A.4a shows the effect of L_1 on ν_P at different strains or net solid fractions. Consistent with the observation in Fig. 8, all samples exhibit similar ν_P irrespective of the degree of deformation. At ε_{eng} = 10% (see Fig. A.3a), or in other words at φ_{net} = 0.16 – 0.17 (see Fig. A.3b), the values of ν_P are mainly in the range of 0.05–0.10, which is also consistent with that of HNPG with different L_2 in Fig. 8 and

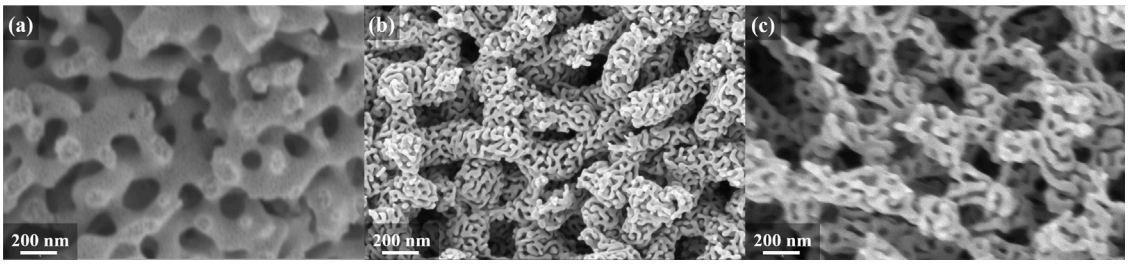

Fig. A.3. SEM images of HNPG samples with same upper level ligament size L_2 = 140 nm and different lower level ligament size L_1. (a) L_1 < 20 nm; (b) L_1 = 20 nm; (c) L_1 = 40 nm.

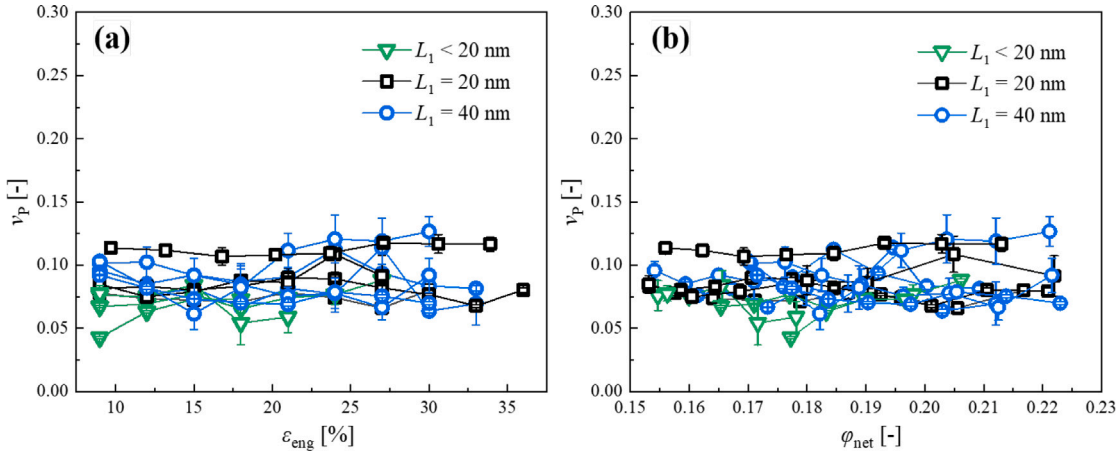

Fig. A.4. The variation of the plastic Poisson's ratio ν_P during compression for hierarchical nanoporous gold with L_2 = 140 nm and L_1 < 20 nm (green triangles), 20 nm (black squares), and 40 nm (blue circles). (a) ν_P vs. engineering strain ε_{eng}; (b) ν_P vs. net solid fraction φ_{net}. Data points include error bars (one standard deviation) for each series.

Fig. 10. The slight difference in ν_P caused by L_1 lies within the bounds of experimental uncertainty and is too small to provide compelling evidence of a definitive size effect.

References

[1] R. Li, K. Sieradzki, Ductile–brittle transition in random porous au, Phys. Rev. Lett. 68 (8) (1992) 1168.

[2] J. Weissmüller, R.C. Newman, H.-J. Jin, A.M. Hodge, J.W. Kysar, Nanoporous metals by alloy corrosion: formation and mechanical properties, Mrs Bull. 34 (8) (2009) 577–586.

[3] H.-J. Jin, J. Weissmüller, D. Farkas, Mechanical response of nanoporous metals: A story of size, surface stress, and severed struts, Mrs Bull. 43 (1) (2018) 35–42.

[4] L.-Z. Liu, X.-L. Ye, H.-J. Jin, Interpreting anomalous low-strength and low-stiffness of nanoporous gold: Quantification of network connectivity, Acta Mater. 118 (2016) 77–87.

[5] L. Lührs, C. Soyarslan, J. Markmann, S. Bargmann, J. Weissmüller, Elastic and plastic Poisson's ratios of nanoporous gold, Scr. Mater. 110 (2016) 65–69.

[6] B. Zandersons, L. Lührs, Y. Li, J. Weissmüller, On factors defining the mechanical behavior of nanoporous gold, Acta Mater. 215 (2021) 116979.

[7] L.-Z. Liu, Y.-Y. Zhang, H. Xie, H.-J. Jin, Transition from homogeneous to localized deformation in nanoporous gold, Phys. Rev. Lett. 127 (9) (2021) 095501.

[8] Y.-Y. Zhang, L. Zou, L.-Z. Liu, H. Xie, C.-H. Li, H.-J. Jin, Mechanical properties of unidirectional nanoporous gold under compression, Acta Mater. 235 (2022) 118078.

[9] S. Sohn, C. Richert, S. Shi, J. Weissmüller, N. Huber, Scaling between elasticity and topological genus for random network nanomaterials, Extrem. Mech. Lett. 68 (2024) 102147.

[10] J. Weissmüller, K. Sieradzki, Dealloyed nanoporous materials with interface-controlled behavior, Mrs Bull. 43 (1) (2018) 14–19.

[11] G. Wittstock, M. Bäumer, W. Dononelli, T. Klüner, L. Lührs, C. Mahr, L.V. Moskaleva, M. Oezaslan, T. Risse, A. Rosenauer, et al., Nanoporous gold: from structure evolution to functional properties in catalysis and electrochemistry, Chem. Rev. 123 (10) (2023) 6716–6792.

[12] Y. Ding, J. Erlebacher, Nanoporous metals with controlled multimodal pore size distribution, J. Am. Chem. Soc. 125 (26) (2003) 7772–7773.

[13] Z. Qi, J. Weissmüller, Hierarchical nested-network nanostructure by dealloying, Acs Nano 7 (7) (2013) 5948–5954.

[14] X. Guo, J. Han, P. Liu, L. Chen, Y. Ito, Z. Jian, T. Jin, A. Hirata, F. Li, T. Fujita, et al., Hierarchical nanoporosity enhanced reversible capacity of bicontinuous nanoporous metal based li-o2 battery, Sci. Rep. 6 (1) (2016) 33466.

[15] T. Juarez, J. Biener, J. Weissmüller, A.M. Hodge, Nanoporous metals with structural hierarchy: A review, Adv. Eng. Mater. 19 (12) (2017) 1700389.

[16] C. Zhu, Z. Qi, V.A. Beck, M. Luneau, J. Lattimer, W. Chen, M.A. Worsley, J. Ye, E.B. Duoss, C.M. Spadaccini, et al., Toward digitally controlled catalyst architectures: Hierarchical nanoporous gold via 3d printing, Sci. Adv. 4 (8) (2018) eaas9459.

[17] C. Wang, Q. Chen, Reduction-induced decomposition: spontaneous formation of monolithic nanoporous metals of tunable structural hierarchy and porosity, Chem. Mater. 30 (11) (2018) 3894–3900.

[18] Y. Shi, Y. Zhang, B. Yu, K. Yin, J. Qin, Z. Zhang, Porous gold with three-level structural hierarchy, Iscience 25 (10) (2022).

[19] S. Shi, Y. Li, B.-N. Ngo-Dinh, J. Markmann, J. Weissmüller, Scaling behavior of stiffness and strength of hierarchical network nanomaterials, Science 371 (6533) (2021) 1026–1033.

[20] L. Riedel, J. Markmann, J. Weissmüller, S. Shi, Tailoring hierarchical nanoporous gold on dual length scales, Phys. Rev. Mater. 7 (11) (2023) 116001.

[21] H. Jeon, J. Markmann, S. Shi, Effects of structural hierarchy and size on mechanical behavior of nanoporous gold, Acta Mater. 273 (2024) 119954.

[22] C.A. Schneider, W.S. Rasband, K.W. Eliceiri, Nih image to imagej: 25 years of image analysis, Nature Methods 9 (7) (2012) 671–675.

[23] L. Lührs, B. Zandersons, N. Huber, J. Weissmüller, Plastic Poisson's ratio of nanoporous metals: A macroscopic signature of tension–compression asymmetry at the nanoscale, Nano Lett. 17 (10) (2017) 6258–6266.

[24] L.J. Gibson, M.F. Ashby, G. Schajer, C. Robertson, The mechanics of two-dimensional cellular materials, Proc. R. Soc. A 382 (1782) (1982) 25–42.

[25] L. Gibson, M. Ashby, Cellular Solids: Structure and Properties, cambridge univ, 1999, Published online.

[26] J. Kováčik, Correlation between Poisson's ratio and porosity in porous materials, J. Mater. Sci. 41 (4) (2006) 1247–1249.

[27] G.E. Dieter, D. Bacon, Mechanical metallurgy, vol. 3, McGraw-hill, New York, 1976.

[28] J. Erlebacher, Mechanism of coarsening and bubble formation in high-genus nanoporous metals, Phys. Rev. Lett. 106 (22) (2011) 225504.

[29] Y. Li, B.-N. Dinh Ngô, J. Markmann, J. Weissmüller, Topology evolution during coarsening of nanoscale metal network structures, Phys. Rev. Mater. 3 (7) (2019).

[30] C. Soyarslan, S. Bargmann, M. Pradas, J. Weissmüller, 3d stochastic bicontinuous microstructures: Generation, topology and elasticity, Acta Mater. 149 (2018) 326–340.
[31] J.R. Davis, Metals Handbook Desk Edition, ASM international, 1998.
[32] N.J. Briot, T. Kennerknecht, C. Eberl, T.J. Balk, Mechanical properties of bulk single crystalline nanoporous gold investigated by millimetre-scale tension and compression testing, Phil. Mag. 94 (8) (2014) 847–866.
[33] T.J. Balk, C. Eberl, Y. Sun, K.J. Hemker, D.S. Gianola, Tensile and compressive microspecimen testing of bulk nanoporous gold, Jom 61 (2009) 26–31.
[34] S. Sun, X. Chen, N. Badwe, K. Sieradzki, Potential-dependent dynamic fracture of nanoporous gold, Nat. Mater. 14 (9) (2015) 894–898.
[35] M. Bürckert, N.J. Briot, T.J. Balk, Uniaxial compression testing of bulk nanoporous gold, Phil. Mag. 97 (15) (2017) 1157–1178.
[36] G. Henkelmann, D. Waldow, M. Liu, L. Lührs, Y. Li, J. Weissmüller, Self-detachment and subsurface densification of dealloyed nanoporous thin films, Nano Lett. 22 (16) (2022) 6787–6793.
[37] Y. Wu, J. Markmann, E.T. Lilleodden, On the consequences of intrinsic and extrinsic size effects on the mechanical response of nanoporous au, Mater. Des. 232 (2023) 112175.
[38] L.-Z. Liu, Y.-Y. Zhang, H.-J. Jin, On correlation between the hardness-to-strength ratio and the plastic Poisson's ratio of nanoporous gold, Mater. Res. Lett. 11 (6) (2023) 454–461.
[39] P. Ahn, O. Balogun, Elastic characterization of nanoporous gold foams using laser based ultrasonics, Ultrasonics 54 (3) (2014) 795–800.
[40] T. Sardhara, A. Shkurmanov, Y. Li, L. Riedel, S. Shi, C.J. Cyron, R.C. Aydin, M. Ritter, Enhancing 3d reconstruction accuracy of fib tomography data using multi-voltage images and multimodal machine learning, Nanomanufacturing Metrol. 7 (1) (2024) 4.
[41] T. Sardhara, A. Shkurmanov, Y. Li, S. Shi, C.J. Cyron, R.C. Aydin, M. Ritter, Role of slice thickness quantification in the 3d reconstruction of fib tomography data of nanoporous materials, Ultramicroscopy 256 (2024) 113878.
[42] K.R. Mangipudi, E. Epler, C.A. Volkert, Topology-dependent scaling laws for the stiffness and strength of nanoporous gold, Acta Mater. 119 (2016) 115–122.
[43] K. Hu, M. Ziehmer, K. Wang, E.T. Lilleodden, Nanoporous gold: 3d structural analyses of representative volumes and their implications on scaling relations of mechanical behaviour, Phil. Mag. 96 (32–34) (2016) 3322–3335.
[44] H. Jeon, N.-R. Kang, E.-J. Gwak, J.-i. Jang, H.N. Han, J.Y. Hwang, S. Lee, J.-Y. Kim, Self-similarity in the structure of coarsened nanoporous gold, Scr. Mater. 137 (2017) 46–49.
[45] J. Bauer, L.R. Meza, T.A. Schaedler, R. Schwaiger, X. Zheng, L. Valdevit, Nanolattices: an emerging class of mechanical metamaterials, Adv. Mater. 29 (40) (2017) 1701850.
[46] J.R. Greer, V.S. Deshpande, Three-dimensional architected materials and structures: Design, fabrication, and mechanical behavior, MRS Bull. 44 (10) (2019) 750–757.
[47] T. Ting, T. Chen, Poisson's ratio for anisotropic elastic materials can have no bounds, Quart. J. Mech. Appl. Math. 58 (1) (2005) 73–82.
[48] H.-J. Jin, L. Kurmanaeva, J. Schmauch, H. Rösner, Y. Ivanisenko, J. Weissmüller, Deforming nanoporous metal: Role of lattice coherency, Acta Mater. 57 (9) (2009) 2665–2672.
[49] C. Volkert, E. Lilleodden, D. Kramer, J. Weissmüller, Approaching the theoretical strength in nanoporous au, Appl. Phys. Lett. 89 (6) (2006).
[50] K. Mangipudi, E. Epler, C. Volkert, On the multiaxial yielding and hardness to yield stress relation of nanoporous gold, Scr. Mater. 146 (2018) 150–153.
[51] A. Hodge, J. Biener, J. Hayes, P. Bythrow, C. Volkert, A. Hamza, Scaling equation for yield strength of nanoporous open-cell foams, Acta Mater. 55 (4) (2007) 1343–1349.
[52] M. Shaw, T. Sata, The plastic behavior of cellular materials, Int. J. Mech. Sci. 8 (7) (1966) 469–478.
[53] R.E. Miller, A continuum plasticity model for the constitutive and indentation behaviour of foamed metals, Int. J. Mech. Sci. 42 (4) (2000) 729–754.